Proceedings of ISERME 2025
19-20 September 2025
https://doi.org/10.31705/ISERME.2025.31

Pore-scale Modelling of Storage and Seepage in the Northern Fuling Shale Gas Field

[*]Yan[1, 2] Y, Li[1] P, Zeng[1] Z and Elakneswaran[2] Y

[1]School of Energy Science and Engineering, Central South University, Changsha, China

[2]Division of Sustainable Resources Engineering, Faculty of Engineering, Hokkaido University, Sapporo, Japan

[*]Corresponding author – yym426880@gmail.com

Abstract

Accurate estimation of shale gas content and production rate is crucial for large-scale shale gas commercialisation. However, limited understanding of shale pore structures and gas accumulation mechanisms has hindered prediction accuracy. This study focuses on the northern Fuling shale gas field in China, where pore size distribution (PSD) models were constructed using literature data. Combined with gas storage and flow behaviour and the phase equilibrium model, a simplified pore structure model was used to develop a storage and seepage model. Results indicate that PSD can be reasonably fitted by both single and segmented curve models. As maximum pore size increases, free gas becomes more dominant and flows mainly in slip flow. Permeability rises linearly with temperature and drops exponentially with pressure, while gas content decreases with temperature and increases with pressure. The material of pore walls significantly influences gas content and apparent permeability, with silicon atoms offering more realistic results. The choice of adsorption model also matters; the Langmuir model yields higher permeability values.

Keywords: Pore size distribution, Shale gas content, Shale permeability, Shale reservoirs

1 Introduction

The technology of extracting shale gas has boomed in the last 30 years [1]. The estimate of gas content and extraction speed becomes essential during the large-scale commercial extraction process [2]. As the storage sites of shale gas, pores play a critical role, but are often overlooked in production due to limited understanding of pore structure and inaccurate adsorption characterisation [3].

According to an existing study, research on shale gas storage and extraction has largely focused on permeability within individual pores. However, the impacts of pore size distribution (PSD) and the number of pores on overall storage and recovery have always been neglected. The commonly used fractal model describing the shale PSD is essentially discontinuous, requiring artificial continuity assumptions during gas storage and flow calculations, which may obscure the role of pore size. Additionally, gas should be affected by limited effects in shale nanopores. The Langmuir model is the most-used model, but not enough to describe gas adsorption in shale pores, especially under high temperatures and pressure, making gas storage and permeability estimates inaccurate. Therefore, the mechanism of gas storage and transformation within the pores needs to be further explored. As methane is the primary shale gas component [4], and experiments in high temperature and high pressure are hard to control [5], theoretical modeling is more reasonable in evaluating the storage and permeability characteristics of shale gas.

In this work, setting the northern Fuling gas field as an example, two PSD models called the single curve model and segment curve model have been

built based on literature data. Meanwhile, a shale gas storage and seepage model was developed based on the PSD-based simplified pore space and phase equilibrium theory. Parametric analyses were carried out with pore size, temperature, pressure, pore wall setting, and adsorption models. During the analysis, all pores were assumed as tortuous, smooth, cylindrical pores with walls of single-component atoms, and fluid molecules were simplified to spheres.

2 Geological setting

Situated in the Upper Yangtze Region, the Fuling gas field is a typical marine shale gas field with significant development potential in China and a diverse geological composition. The field is divided into two segments by the Shimen fault, and wells JY-1, JY-2, JY-A, and JY-B etc., serve as main wells in the northern Fuling gas field [6]. Located at 2000–4000 m between the Silurian and Ordovician, the northern part of the shale formations can be further categorised into Long1, Long2, Long3, and other groups. The shale formations there are overmature.

3 Materials and Methods

3.1 Data collection

To ensure characterising pores in the northern Fuling gas field accurately, data pertaining to 37 samples from the Wufeng–Longmaxi formation were collected from the literature, mostly reported at depths of 2200–3650 m. For the accumulated volume V of pores whose size is less than D, the derivative in D is used to express PSD, meaning

$$f(D)=\frac{\mathrm{d}V}{\mathrm{d}D} \tag{1}$$

3.2 Integral median processing method

As the sample data obtained from the literature were diverse, these data could be homogenised and simplified by taking the median of the integrals. For the pore volume between D_1 and D_2 ($D_1 < D_2$), by the integral mean value theorem, there must exist D_ξ satisfying

$$f(D_\xi)=\frac{\int_{D_1}^{D_2} f(D)\mathrm{d}D}{D_2\text{-}D_1} \tag{2}$$

$f(D_\xi)$ can approximately express the variation of the PSD curve in the [D_1, D_2] section. Here, we proposed D_ξ' to approximate D_ξ, and D_ξ' will be

$$D_\xi'=\frac{D_1+D_2}{2}\approx D_\xi \tag{3}$$

The $f(D_\xi')$ may not be entirely accurate, but it is sufficient to approximate the variation of the PSD curve. This median processing method was applied to standardise the transverse coordinates of each curve. By taking medians of dV/dD values within the same pore size range, the influence of outliers was reduced, making the approximation of the PSD robust. This resulting curve, termed the characterised PSD curve, represents the overall pore structure of the northern Fuling shale sample and is used for subsequent fitting.

3.3 Fitting models

In this work, two approaches were employed to fit the characterised PSD curve. Pore structures were modelled using representative PSD data, fitted with single and segmented curve models to capture multi-scale heterogeneity. The latter one divided the characterised PSD curve into two parts at D=1 nm and represented each part with different models. The models used in this work are listed in Table 1. Some models were modified to better align with the actual conditions of shale pores [7].

Table 1: PSD models

Method	Model
Single Curve Models	Pearson IV
	Pearson VII
	Gamma
	GaussMod
Segment Curve Models (for D<1 nm)	Log-Normal
	Gaussian
	Lorentz
	ECS
Segment Curve Models (for D>1 nm)	Allometric
	Jaky
	Weibull
	Log-Weibull
	ExpDec2

3.4 Fitting evaluation

There are various methods for evaluating the accuracy of a fitting function. In the ideal case, a good fit function should have fewer parameters, a higher R^2 value, a lower p value, and a smaller mean squared error (MSE).

The logarithmic mean absolute percentage error (LogMAPE, Eq.4) and logarithmic median absolute percentage error (LogMedAPE, Eq.5) were employed to quantify the deviations between the predicted and actual values for each sample. These two indices robustly quantify the deviations between predicted and actual values:

$$\varepsilon_{\mathrm{LogMAPE}}\left(D_{\xi}^{'}\right)=\frac{1}{n}\sum_{i=1}^{n}\left|\log\left(\frac{f_{\mathrm{pred},i}\left(D_{\xi}^{'}\right)}{f\left(D_{\xi}^{'}\right)}\right)\right| \quad (4)$$

$$\varepsilon_{\mathrm{LogMedAPE}}\left(D_{\xi}^{'}\right)=\mathrm{Med}\left(\left|\log\left(\frac{f_{\mathrm{pred},i}\left(D_{\xi}^{'}\right)}{f\left(D_{\xi}^{'}\right)}\right)\right|\right) \quad (5)$$

Where Med(a) is used to determine the median number. Since the deviations are obtained on different segments of pore size, the deviations of each segment vary obviously. Consequently, the weighted average deviation $\varepsilon_{\mathrm{full}}$ was used to represent the overall bias incurred.

$$\varepsilon_{\mathrm{full}}=\frac{\Sigma\varepsilon\left(D_{\xi}^{'}\right)(D_2-D_1)}{\Sigma(D_2-D_1)} \quad (6)$$

3.5 Simplified shale pore space

In this work, all the pores are regarded as tortuous, smooth cylindrical, which means the length of the pores is more than the shale size in the flow direction. Fig. 1 shows a simplified shale space. A simplified shale pore model was built to represent the shale pore space. When dD is small enough, the pore size between D and D+dD can be regarded as D. Also, according to the definition of $f(D)$, there is

$$\mathrm{d}V=\frac{\pi}{4}D^2L\mathrm{d}N=\rho_{\mathrm{s}}Aaf(D)\mathrm{d}D \quad (7)$$

Where L is the length of pores whose size is D, and N is the accumulated number of pores. Both L and N are functions of D [8]. A is the cross-sectional area of the shale sample, and a is the sample's size in the flow direction. With this equation N should fit:

$$\mathrm{d}N=\frac{4\rho_{\mathrm{s}}Aaf(D)}{\pi D^2L}\mathrm{d}D \quad (8)$$

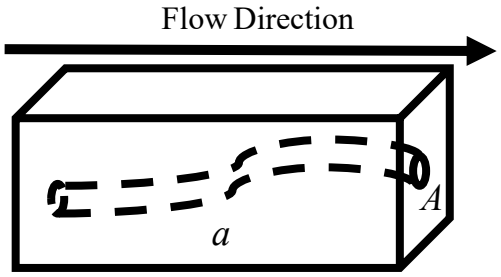

Figure 1: The PSD curves of some typical samples.

4 Method for shale gas content and permeability model

4.1 Adsorption effect, gas coverage, and gas velocity

With the phase equilibrium model, the adsorption effect can be described mathematically. For a pore whose size is D, and at a certain temperature and pressure, the adsorption layer r_{ad} can be obtained. The gas coverage, meaning the proportion of the real adsorption amount and the theoretical adsorption amount, can also be obtained:

$$D_{\mathrm{e}}=D-2r_{\mathrm{ad}} \quad (9)$$

$$\theta=\frac{\frac{\pi}{4}\left(D^2-D_{\mathrm{e}}^2\right)\rho_{\mathrm{ad}}L}{\frac{\pi}{4}\left(D^2-(D-6\delta)^2\right)\rho_{\mathrm{ad}}L}=\frac{r_{\mathrm{ad}}(D-r_{\mathrm{ad}})}{3\delta(D-3\delta)} \quad (10)$$

While δ is the methane molecule collapse diameter.

Regarding the velocity of the gas, the Lee-Gonzalez-Eakin function was usually used during relative research. In this work, a modified version [9] was used because of high-pressure conditions.

4.2 Gas transport regime in a single pore

Gas transport in a pore contains slip flow, transition flow, free molecular flow, and surface diffusion. The slip flow mass flux, the free molecular flow mass flux, and the surface diffusion flow mass flux can be obtained by

$$J_{\mathrm{S}}=F\frac{PM_{\mathrm{g}}}{ZRT}\frac{D_{\mathrm{e}}^2}{32\mu_{\mathrm{g}}}\frac{\Delta P}{L} \quad (11)$$

$$J_{\mathrm{N}}=\frac{D_{\mathrm{e}}}{3}C_{\mathrm{g}}\left(\frac{8ZM_{\mathrm{g}}}{\pi RT}\right)^{\frac{1}{2}}\frac{P}{Z}\frac{\Delta P}{L} \quad (12)$$

$$J_{\mathrm{B}}=D_{\mathrm{B}}\frac{C_{\mathrm{SC}}}{P}\frac{\Delta P}{L} \quad (13)$$

While F is a fixed factor [5], [10], C_{g} (Pa^{-1}) is a coefficient. D_{B} (m^2/s) is the surface diffusion coefficient. C_{SC} (kg/m^3) is the adsorbed gas concentration. Both D_{B} and C_{SC} are linked to the gas condition [11], [12].

The transition flow is the most complicated part of the flow regime. In this work, it is regarded as a combination of slip flow and free molecular flow. The flow caused by different pressure is [8]

$$J_{\mathrm{F}}=\frac{1}{1+\mathrm{Kn}}J_{\mathrm{S}}+\frac{1}{1+\mathrm{Kn}}\mathrm{J_N} \quad (13)$$

While Kn is the Knudsen number.

4.3 Total gas flux and apparent permeability

Mass flux refers to the mass flow per unit area in a pore, and the total flow in bulk shale results from contributions across pores of varying sizes. Based on this and the definition of permeability, the total mass flow can also be calculated by

$$Q=\int_{D_{\min}}^{D} J\frac{\pi D_e^2}{4}\mathrm{d}N=\frac{KA}{\mu_g}\frac{PM_g}{ZRT}\frac{\Delta P}{a} \tag{15}$$

Adding these functions together, the apparent permeability can be described as the sum of slip flow permeability, free molecular flow permeability, and surface diffusion permeability. In this research, Python programming was used for the computations. Fig. 2 shows the calculation process.

$$K_{app}=K_S+K_N+K_B \tag{16}$$

$$K_S=\frac{F\rho_s a^2}{32}Z\int_{D_{\min}}^{D}\frac{D_e^5 f(D)}{D^2L^2(D_e+\lambda)}\mathrm{d}D \tag{17}$$

$$K_N=\frac{\lambda}{3}\rho_s a^2\left(\frac{8RT}{\pi M_g}\right)^{\frac{1}{2}}\mu_g C_g\int_{D_{\min}}^{D}\frac{D_e^3 f(D)}{D^2L^2(D_e+\lambda)}\mathrm{d}D \tag{18}$$

$$K_B=4\rho_s a^2 D_B^0\frac{RT}{P^2}\frac{1}{\pi\delta^3 N_A}Z\mu_g\int_{D_{\min}}^{D}\frac{\eta\theta D_e^2 f(D)}{D^2L^2}\mathrm{d}D \tag{19}$$

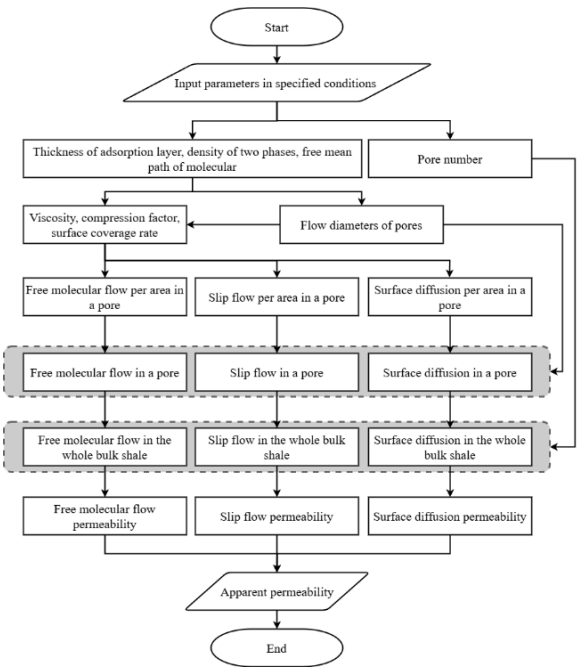

Figure 2: The structure of the permeability calculation model.

4.4 Shale gas content

For cylinder pores, the adsorption gas and free gas in a pore can be obtained as

$$N_{ads}=\frac{\pi}{4}\left(D^2-(D-2r_{ad})^2\right)\rho_{ad}L \tag{20}$$

$$N_{fs}=\frac{\pi}{4}(D-2r_{ad})^2\rho_f L \tag{21}$$

The total adsorption gas N_{ad}, the total free gas N_f, and the total gas N can be calculated as

$$N_{ad}=\rho_s Aa\int_{D_{\min}}^{D}\frac{D^2-(D-2r_{ad})^2}{D^2}\rho_{ad}f(D)\mathrm{d}D \tag{22}$$

$$N_f=\rho_s Aa\int_{D_{\min}}^{D}\frac{(D-2r_{ad})^2}{D^2}\rho_f f(D)\mathrm{d}D \tag{23}$$

$$N=N_{ad}+N_f \tag{24}$$

4.5 Standard condition

In the Fuling gas field, the temperature and pressure change when the depth increases [13]. In this work, 2400 m is set as the standard condition of shale in the northern Fuling gas field. All parameters are shown in Table 2.

Table 2: Fitting results of single curve models

Variable	Value
Depth of sample (m)	2400
Crossing area of shale (m^2)	100
Length of shale (m)	10
Pore wall material	Si
Pressure difference (MPa)	5
Minimum pore size (nm)	4
Maximum pore size (nm)	100
Gas slip constant	-1
Ratio of the plugging rate constant and the forward migration rate constant	0.5
Heat of adsorption of the isotope when the gas coverage is 0 (J/mol)	16000
Density of shale (kg/m^3)	2.57×10^3
Porosity (%)	3.7867
Shale gas	100% methane
Mole mass of methane (g/mol)	16.0428
Collapse diameter of the methane molecule (nm)	0.39
Critical temperature of methane (K)	190.564

Critical pressure of methane (MPa)	4.5989
Eccentricity factor of methane	0.01155

5 Results and discussion

5.1 PSD models

5.1.1 Fitting results for single curve models

Fig. 3 shows the results of fitting the characterised PSD curves with four models. It is observed that Pearson IV and Pearson VII have better fitting performances than GaussMod and Gamma models. Table 3 shows the fitting results and accuracy of these three models. On balance, the Pearson IV model is significantly simplified to describe the shale pore volume in the northern Fuling gas field.

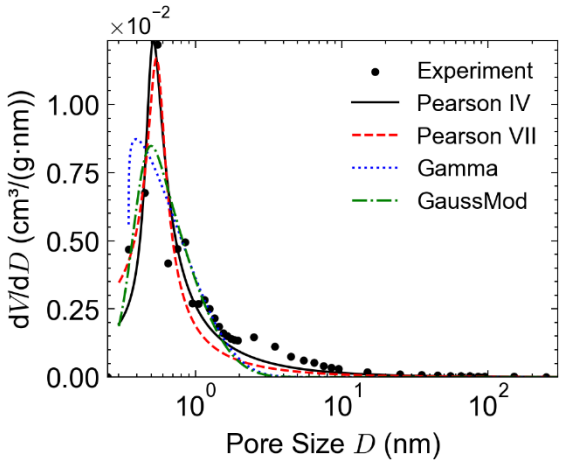

Figure 3: Performance of single curve models fitted to characterised PSD curve.

Table 3: Fitting results of single curve models

Model	R^2	*P* value	MSE
Pearson IV	0.893	0	2.063E-5
Pearson VII	0.835	7.105E-15	3.274E-5
Gamma	0.807	8.860E-14	3.839E-5
GaussMod	0.823	2.154E-14	3.511E-5

5.1.2 Fitting results for segment curve models

Fig. 4 shows the results of fitting the characterised PSD curve. For the section with the pore size below 1 nm, Table 4 shows the fitting results and accuracy of the models. The Log-Normal, Gaussian, and Lorentz models present relatively similar results. The ECS model shows better fitting performance, which is also reflected in the R^2 and the RSS. Thus, the ECS model is suitable for describing and predicting the shale PSD for the section when the pore size is below 1 nm. For the section with the pore size over 1 nm, as there is no significant difference when fitting, all these models can be used to describe and predict the characterised PSD curve for the section with the pore size over 1 nm.

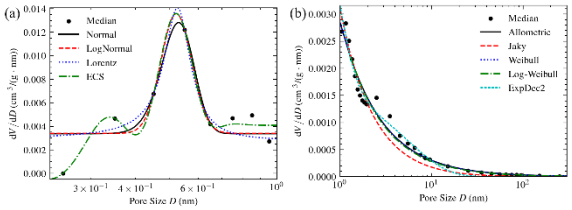

Figure 4: Performance of segment curve models fitted to characterised PSD curve.

Table 4: Fitting results of segment curve models (pore size below 1 nm)

Model	R^2	*P* value	MSE
For pore size $D < 1$ nm			
Log-Normal	0.455	0.023	2.781E-5
Gauss	0.643	0.012	1.754E-5
Lorentz	0.667	0.010	1.636E-5
ECS	0.884	0.028	2.953E-6
For pore size $D > 1$ nm			
Allometric	0.972	0	6.134E-7
Jaky	0.961	1	9.032E-7
Weibull	0.972	0	6.135E-7
Log-Weibull	0.972	0	6.126E-7
ExpDec2	0.980	0	4.049E-7

5.1.3 Deviation analysis

Deviations between actual pore volumes and model predictions were calculated. The Jaky and ExpDec2 models show rapidly increasing deviations with pore size, indicating their unsuitability for shale characterisation. Table 5 presents deviations for other models. The ECS model shows relatively large errors, likely due to volume fluctuations below 1 nm and possible capillary condensation. The LogMAPE and LogMedAPE values of the Log-Weibull and Allometric models are 24.58% and 24.01%, respectively, indicating higher reliability than the Weibull model. The Pearson IV model also shows acceptable deviations.

Table 5: Fitting results of segment curve models (pore size over 1 nm)

Model	LogMAPE (%)	LogMedAPE (%)
Pearson IV	34.22	30.15

ECS	74.41	73.75
Allometric	25.71	24.01
Weibull	29.83	25.90
Log-Weibull	24.58	25.47

5.2 Influence of pore size on shale apparent permeability

Apparent permeability is affected by various factors. In this work, apparent permeability is modeled as a function of pore size, specifically representing the permeability of bulk shale when pores larger than the given diameter D are considered blocked. As the minimum pore size is 4 nm, the Allometric PSD model was employed to characterise the pore structure. The variation of permeability change with pore size is shown in Fig. 5. In the figure, K_S, K_N, and K_B represent the permeability contributed by slip flow, free molecular flow, and surface diffusion, respectively. K_D is the Darcy permeability, and K is the total apparent permeability.

Slip flow dominates gas transport, exceeding other mechanisms by orders of magnitude. Surface diffusion permeability is consistently higher than free molecular flow. When the maximum pore size is below 20 nm, non-Darcy effects remain significant. Slip flow becomes predominant as pore size increases, indicating that large pores influence apparent permeability more despite the abundance of smaller pores.

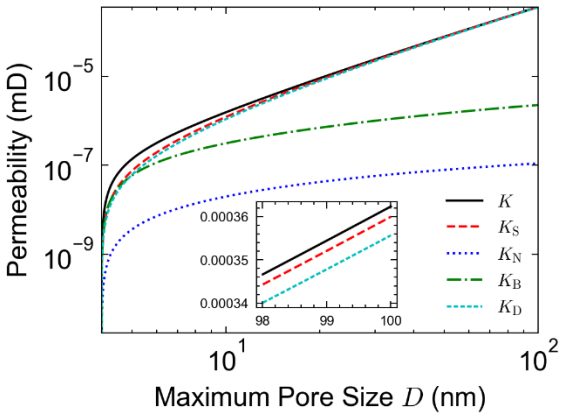

Figure 5: Different kinds of shale permeability changed with the maximum pore size.

5.3 Influence of the pore size on shale gas content

Gas content is also a key factor during shale gas production. The accumulated adsorption gas and free gas content with maximum pore size increase are shown in Fig. 6. In the figure, V_A and V_F mean the volume of adsorption gas and free gas, and their sum V is the total gas content.

The total gas content increases approximately linearly with the logarithm of the maximum pore size. Adsorption gas dominates in pores less than 12.45 nm, but as the pore size increases, free gas continues to increase significantly, while adsorption gas increases more slowly due to the limited thickness of the adsorption layer in larger pores. Overall, free gas accounts for nearly 80% of the total gas content in shale, but the contribution from adsorption gas in small pores remains significant.

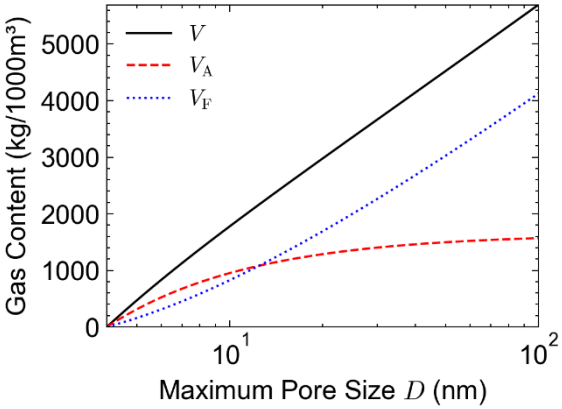

Figure 6: Different kinds of gas content with the maximum pore size.

5.4 Influence of temperature and pressure on apparent permeability and gas content

The change in pressure and temperature can lead to a change in permeability and gas content volume. In this part, for the 2400 m shale sample in the northern Fuling gas field, the pressure is 37.03 MPa and the temperature is 361.07 K. One of the pressures or temperatures is fixed to analyse the effect of the other factor. The result obtained is shown in Fig. 7. The result shows that when the temperature rises, the permeability rises linearly, and the gas content decreases linearly. Correspondingly, when the pressure rises linearly, the permeability decreases exponentially, and the gas content increases linearly. The regression functions are

$$K_{app}=3.17\times10^{-4}+1.26\times10^{-7}T \quad (25)$$

$$K_{app}=3.61\times10^{-4}+1.78\times10^{-4}\times\exp\left(-\frac{P}{7.76}\right) \quad (26)$$

$$V=11932.01-17.16T \quad (27)$$

$$V=2181.61+94.40P \quad (28)$$

In these functions, V (kg/1000m^3) means the total shale gas content; K (mD) means the apparent permeability; P (MPa) is the pressure; T (K) is the temperature. These functions all have R^2 over 0.95, showing their accuracy.

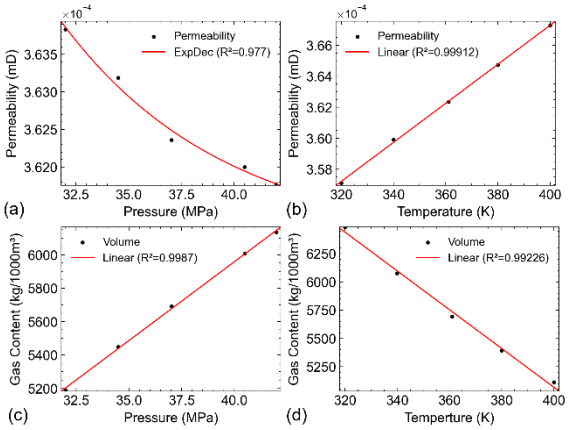

Figure 7: The relationship between (a) permeability and pressure; (b) permeability and temperature; (c) gas content and pressure; (d) gas content and temperature.

5.5 Influence of pore wall material

In this study, pore wall materials are simplified to single-atom types, as methane interacts differently with various atoms. In shale, the main constituent elements include C, Si, Fe, Al, Ca, and O, while oxygen atoms typically form oxides by bonding with metal ions and do not directly participate in gas adsorption. With the assumption of the component in shale listed in Table 6 and the data collected from the northern Fuling gas field, the elemental proportion can be estimated as C: Si: Fe: Al: Ca = 0.05: 0.65: 0.03: 0.21: 0.06.

In Fig.8, simulation results under single-element pore wall assumptions are compared to a mixed condition, which assumes that pores of each size are distributed across wall atom types according to the specified ratio. The percentage deviation from the mixed condition is shown on each bar. Silicon wall assumption shows the most favorable outcome, with 0.11% lower apparent permeability and 0.13% higher gas content than the mixed case. These differences are attributed to the effect of wall material on adsorption layer thickness. Thicker layers reduce effective flow area, lowering permeability. This result is consistent with previous studies [4].

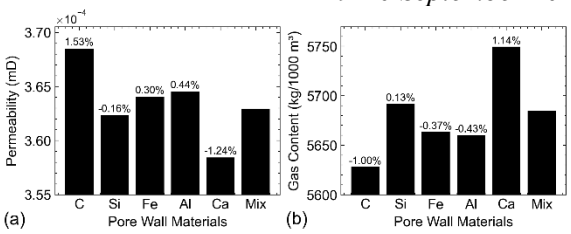

Figure 8: The (a) permeability and (b) gas content results based on different pore wall material assumptions.

Table 6: Approximate rules of compounds in shale

Mineral	Main part
Quartz	SiO_2
Feldspar	SiO_2, Al_2O_3, K_2O, Fe_2O_3, Na_2O, CaO each 1/6
Carbonate mineral	$CaCO_3$
Pyrite	FeS_2
Clay	$Al_4[Si_4O_{10}](OH)_8$

5.6 Influence of adsorption model on apparent permeability

Compared to the Langmuir model, the phase equilibrium model offers a more accurate description of shale adsorption behavior, meaning more reliable permeability estimates. In the Langmuir model, key parameters such as gas coverage, flow diameter, and adsorption layer thickness are derived via the Langmuir pressure. For the northern Fuling gas field, the Langmuir pressure can be calculated [13]. With the gas coverage derived, the pore flow diameter is

$$D_e=D-2\delta\theta \tag{29}$$

Fig. 9 shows the permeability values obtained under different adsorption models for shale at a depth of 2400 m. The permeability based on the Langmuir model is 9.69% larger than the phase equilibrium model. Langmuir adsorption is a monolayer, resulting in a thinner adsorption layer and thus a larger flow diameter. In contrast, the phase equilibrium model accounts for multilayer adsorption and avoids indirect estimation, enhancing accuracy.

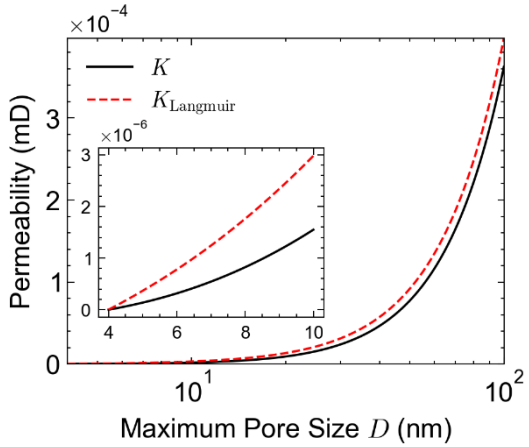

Figure 9: Permeability obtained by using the Langmuir and the phase equilibrium model.

6 Conclusions

This study investigated shale gas storage and seepage behaviour in the northern Fuling gas field by pore-scale modelling. Representative PSD curves were derived and fitted by multiple models, among which the Pearson IV, Log-Weibull, and Allometric models showed good agreement with experimental data. Coupling these PSD models with phase equilibrium and flow theories revealed that slip flow dominates transport, particularly in larger pores, which significantly influence apparent permeability despite their low abundance. For adsorption behaviour, small pores weigh a lot. Permeability decreases with pressure and increases with temperature, while gas content shows opposite trends. The phase equilibrium model provided more accurate permeability estimates than the Langmuir model by better accounting for adsorption layer effects.

Acknowledgements

This work was supported by the National Natural Science Foundation of China (Grant No. 52074348).

References

[1] X. Ma et al., "Prospects and challenges of shale gas development in China", *Petroleum Science Bulletin*, vol. 8, no. 4, pp. 491–501, 2023.

[2] O. Iqbal, E. Padmanabhan, A. Mandal, and J. Dvorkin, "Characterisation of geochemical properties and factors controlling the pore structure development of shale gas reservoirs", *Journal of Petroleum Science and Engineering*, vol. 206, Nov. 2021, Art. no. 109001.

[3] P. Zhang et al., "Pore Structure and Fractal Character of Lacustrine Oil-Bearing Shale from the Dongying Sag, Bohai Bay Basin, China", *Geofluids*, vol. 2021, pp. 1–19, July 2021.

[4] X. She et al., "Tectonic characteristics and their shale gas geological significance of the Mesozoic-Paleozoic in Jiaoshiba area, the Sichuan Basin", *Oil & Gas Geology*, vol. 37, no. 6, pp. 828–837, 2016.

[5] H. Bayat, M. Rastgou, A. Nemes, M. Mansourizadeh, and P. Zamani, "Mathematical models for soil particle-size distribution and their overall and fraction-wise fitting to measurements: Effect of textural fractions on accuracy of PSD models", *Eur J Soil Sci*, vol. 68, no. 3, pp. 345–364, May 2017.

[6] Q. Wang, Y. Hu, J. Zhao, L. Ren, C. Zhao, and J. Zhao, "Multiscale Apparent Permeability Model of Shale Nanopores Based on Fractal Theory", *Energies*, vol. 12, no. 17, pp. 3381, Sept. 2019.

[7] A. Viswanathan, "Viscosities of natural gases at high pressures and high temperatures", M.S. thesis, Texas A&M University, Texas, USA, 2007.

[8] K. Wu, Z. Chen, and X. Li, "Real gas transport through nanopores of varying cross-section type and shape in shale gas reservoirs", *Chemical Engineering Journal*, vol. 281, pp. 813–825, Dec. 2015.

[9] A. Beskok and G.E. Karniadakis, "A Model for Flows in Channels, Pipes, and Ducts at Micro and Nano Scales", *Microscale Thermophysical Engineering*, vol. 3, no. 1, pp. 43–77, Feb. 1999.

[10] Y. Pang, M. Y. Soliman, H. Deng, and X. Xie, "Experimental and analytical investigation of adsorption effects on shale gas transport in organic nanopores", *Fuel*, vol. 199, pp. 272–288, July 2017.

[11] W. Song et al., "Apparent gas permeability in an organic-rich shale reservoir", *Fuel*, vol. 181, pp. 973–984, Oct. 2016.

[12] Q. Gou et al., "Quantitative calculated shale gas contents with different lithofacies: A case study of Fuling gas shale, Sichuan Basin, China", *Journal of Natural Gas Science and Engineering*, vol. 76, Apr. 2020, Art. no. 103222.

[13] Y. Chen, H. Zhan, and Z. Zeng, "Thermodynamic modeling for confined fluids in nanopores using an external potential-advanced equation of state", *Journal of Natural Gas Science and Engineering*, vol. 101, May 2022, Art. no. 104519.